Solution structure and synaptic analyses reveal molecular mechanisms of bispecific T cell engagers

Authors: Oskar Staufer[1, *], Alexander Leithner[1, *], Falk Liberta[2], Sally Zhou[3], Felix Schiele[2], Sophia Reindl[2], Herbert Nar[2], Stefan Hoerer[2], Maureen Crames[3], Stephen Comeau[3], David Young[3], Sarah Low[3], Edward Jenkins[4,5], Simon J. Davis[4,5], David Klenerman[6], Andrew Nixon[3], Noah Pefaur[3], David Wyatt[2], Srinath Kasturirangan[3], Michael L. Dustin[1]

* contributed equally

Corresponding author: Michael.dustin@kennedy.ox.ac.uk

Affiliations:

1: The Kennedy Institute of Rheumatology, University of Oxford, OX3 7FY, Oxford, United Kingdom

2: Boehringer Ingelheim Pharma GmbH & CO. KG, Birkendorfer Strasse 65, 88397 Biberach an der Riss, Germany

3: Biotherapeutics Discovery, Boehringer Ingelheim, Ridgefield, CT, 06877, USA

4: Medical Research Council Human Immunology Unit, University of Oxford, OX3 9DU, Oxford, United Kingdom

5: Radcliffe Department of Medicine, University of Oxford, OX3 9DU, Oxford, United Kingdom

6: Yusuf Hamied Department of Chemistry, University of Cambridge, Cambridge, CB2 1EW, United Kingdom

Classification: Biological Science, Immunology and Inflammation

Keywords: Immunological Synapse, Breast Cancer, Supported Lipid Bilayers, Immunotherapy

Abstract:

Bispecific T-cell engagers (TcEs) link the T-cell receptor to a tumour associated antigen on cancerous cells to form a tumoricidal immunological synapse (IS). To gain insight into TcE performance, we investigated four TcE formats (A-D) that link the CD3ε N-terminus to a membrane proximal site in Her2. The spacing between CD3ε and Her2 was increased in ~4 nm steps (A<B<C<D) through combinations of single-chain variable fragments (scFv) and antigen-binding fragments (Fab), linked to the hinge of the crystallizable fragment (Fc), or by linking an scFv to the base of the Fc. TcEs mediated equivalent adhesion, but cytotoxic potency followed A>B=C>D. To measure the TcE-determined distance between the membrane anchoring sites of CD3ε and Her2 we performed small angle X-ray scattering

(SAXS), revealing sub-13 nm distances for Formats A and B, but larger distances for C and D (≥18 nm). IS-parameters for A-C included similar close membrane apposition, fast IS formation and robust CD45 exclusion, whereas D displayed greater membrane separation, slow IS formation, and modest CD45 exclusion. TcE recruitment of co-stimulatory CD2-CD58 interactions followed the relationship A>B>C>D. Our results suggest a sequence of events, mediated by TcEs: 1.) adhesion, 2.) CD45 exclusion and 3.) co-stimulation recruitment. The most potent Format (A) performs 1-3, the intermediate Formats (B-C) fully achieve 1-2, and the least effective Format (D) reaches only 1. We speculate that the 18 nm-distance complex, formed by Format C, used in approved TcEs, undergoes tilting in the IS to exclude CD45, but this is suboptimal for CD2-CD58 recruitment.

Significance statement:

Bi-specific T-cell engagers (TcEs) are immunotherapeutic drugs against cancer. Structurally, they are based on antibodies and are engineered to simultaneously bind specific molecules on T-cells and tumour cells. This results in the formation of an immunological synapse (IS), and killing of the tumour cell by the T-cell. We designed a panel of TcEs with varying distances between their T-cell and tumour cell binding sites and subjected it to structural characterisation and microscopy-based analysis of IS formation with a lipid bilayer system. We identify a sequence of events for an increasingly successful TcE: 1.) mediate adhesion, 2.) exclude CD45, and 3.) recruit co-stimulation. These steps establish quantitative criteria for the design and testing of future TcEs and the advancement of immunotherapy.

Introduction:

The past decade has witnessed a transition from systemic drugs that target tumors broadly, towards immunotherapies that specifically modulate immune responses against cancerous cells. Checkpoint inhibitors, that block inhibitory immune signaling, and genetically engineered T cells, that express artificial T cell-activating receptors for targeted cancer cell killing, have joined the conventional arsenal of surgical resection, chemotherapy, and irradiation (1). Additionally, bispecific T cell engagers (TcE) that are able to simultaneously bind to epitopes on cancer cells and T cells, have gained significant clinical interest as they represent a versatile, highly-potent and economical immunotherapeutic tool (2). TcEs are antibody-derived molecules harboring at least one antigen binding site (paratope) that is selective for T cells, typically directed against CD3ε of the T cell receptor (TCR) complex, while the other paratope is targeted against a tumor associated antigen (TAA). A plethora of TcE-designs have been developed (3) that can be subcategorized into those retaining the Fc-region of IgGs

and those that feature only minimal antigen binding arms. In both cases, the paratope carrying units are typically linked by at least one flexible hinge or spacer. While Fc-less bispecific formats show improved penetration of solid tumors, Fc-containing TcEs feature improved pharmacokinetic characteristics, such as extended circulation half-life, and better chemistry, manufacturing, and control characteristics. Mechanistically, TcEs physically link polyclonal effector T cells with cancer cells to promote the formation of cytolytic immunological synapses (IS), exploiting the intrinsic cytotoxic machinery of T cells for a therapeutic benefit (4). Since the first-in-class approval of blinatumomab in 2015, a large variety of different TcE formats were (pre-) clinically assessed in solid and hematological tumors (5), particularly for lymphoblastic leukemia and Her2^{+} solid tumors (2). These assessments revealed significant variations in TcE efficacy and safety. Extensive research efforts revealed that the pharmacodynamics and kinetics of TcEs are regulated by a variety of factors such as TcE architecture, i.e. orientation and spacing of paratopes as well as overall TcE configuration, binding affinity and valency, and Fc-design (5–7).

IS formation between T cells and target cells is a highly orchestrated process, dominated by a complex interplay of molecular self-assembly events and active cellular rearrangements. IS structure, maturation and signaling have been reviewed in detail elsewhere (8). Central structural elements underlying antigen recognition and signal integration at the IS include a TCR-enriched and filamentous-actin (F-actin) depleted central supramolecular activation cluster (cSMAC), integrin lymphocyte function-associated antigen 1 (LFA-1) – intercellular adhesion molecule 1 (ICAM1) based peripheral adhesion sites (pSMAC) and a distal (dSMAC) region that concentrates proteins with large ectodomains (ECDs), such as CD45 and CD43, and is a site of F-actin polymerization. Additionally, the dSMAC also accumulates interactions of the co-stimulatory receptor CD2 on T cells with its ligand CD58 in a large contact, referred to as the corolla (9). Interestingly, this form of IS organization appears to be maintained in some TcE-mediated synapses (10).

One model that has proven useful in understanding TCR-triggering is kinetic-segregation (KS) (11). This model is based on the close proximity of approximately 13-14 nm between the two cellular membranes (12, 13). This allows for the interaction of TCR-peptide-major histocompatibility complexes (pMHC) and co-stimulatory receptor-ligand pairs, including CD2-CD58, resulting in the exclusion of transmembrane tyrosine phosphatases with large ECDs, such as CD45, from the cell-cell contact site. CD45 exclusion leads to locally increased phosphorylation of pMHC-bound TCRs and promotes downstream signaling for T cell activation. Importantly, it is known that CD45 is not efficiently excluded from T cell contacts separated by a distance of 18 nm (13). CD45 exclusion is particularly important for signaling at low TCR-ligand density, and high ligand density can overcome the need for CD45 exclusion,

based on a model with full 3D control of anti-CD3 Fab positioning in the IS (14). Consistent with this model of passive exclusion of large inhibitory membrane proteins, effective TcE-mediated IS formation is accompanied by CD45 exclusion, wherefore TcEs that target membrane distal epitopes of large TAAs show reduced cytotoxic potency (15, 16).

However, while the last decades of extensive research on natural IS formation have brought a detailed understanding of its maturation and signaling, the mechanisms of TcE-mediated IS formation have only been addressed by a small number of studies (4–7, 10, 15, 16). Consequently, several questions of fundamental relevance for TcE-based therapeutic design remain: to what degree is the physiological IS organization maintained in the TcE-mediated IS? How does TcE design impact on the dynamics of IS formation, TCR-signaling strength and exclusion of proteins with large ECDs? How do different TcE formats arrange receptors in space and how do these complexes fit into close contacts? And can the efficiency of a given TcE be predicted from its structure and performance in reductionistic experimental settings?

To address these questions, we combined functional cell-based assays, structural analysis of TcE-CD3ε-TAA complexes in solution through small-angle X-ray scattering (SAXS), and a reductionistic supported lipid bilayer (SLB) system that we adapted to present Her2 as a model TAA. SLBs are well established as effective surrogates of antigen-presenting cells (APC) with excellent optical properties that allow high-resolution imaging (17). This allowed us to study synapses formed between T cells or T cell-mimicking giant unilamellar vesicles (GUVs) and cancer cell-mimicking SLBs, for a set of four well-characterized TcEs with varying paratope spacings, allowing extraction of the quantitative parameters underpinning signaling at the TcE IS. We found that in-solution structure, analysis of TcE mediated membrane apposition, and the ability to recruit CD2-CD58 co-stimulation at the IS, give complementary information that together provide insight into factors controlling TcE potency: sequential requirements to 1.) mediate adhesion, 2.) exclude inhibitory proteins with large ECDs, like CD45, and 3.) recruit CD2-CD58.

Results:

We began our study by designing a panel of four different bispecific TcEs, termed Formats A-D, with an estimated (18) maximum paratope-spacing ranging from 10 to 22 nm (**Fig.1A**). TcEs were engineered by knob-into-hole (19) technology for monovalent binding of membrane proximal domain IV of human Her2 (20) on tumour cells and human CD3ε N-terminal peptide (21) on T cells, respectively. All TcEs were monomeric by size exclusion chromatography with the expected hydrodynamic radii **(Supplementary Figure 1A and E).** TcEs that included single-chain variable fragments (scFvs), that is A, B and D, had greater hydrophobicity

according to hydrodynamic interaction chromatography and lower thermal stability based on differential scanning calorimetric analysis **(Supplementary Figure 1B and C).** All TcEs bound Her2 with high affinity and there was no dissociation in the time frame of the experiment according to biolayer interferometry measurements. However, Formats C and D had lower affinity for Her2 based on surface plasmon resonance, although still in the low pM range **(Supplementary Figure 1D and E)**. This led us to also generate versions of Formats B and C with lower affinity for the TAA, referred to as B-L and C-L, respectively, to test the importance of this parameter **(Supplementary Figure 1E).**

Next, we performed functional analysis to assess the cytotoxic potency of the different TcE formats in breast cancer cell-line and primary, activated human $CD8^+$ T cell co-cultures. In order to evaluate the impact of Her2 surface expression on cancer cells, which is a pivotal factor for TcE on-target/off-tumor targeting (22), we included two cell lines with varying Her2 membrane densities in our analysis: BT474 ductal carcinoma breast cancer cells, with ~$6x10^5$ molecules Her2/cell ($Her2^{high}$), and MCF-7 mammary epithelium adenocarcinoma cells, with ~$2x10^4$ Her2/cell ($Her2^{low}$) (23). We further verified that co-stimulatory ligands ICAM1, CD58 (LFA-3) and CD80 were expressed on both cell lines at comparable levels (**Supplementary Figure 2A**). Cytotoxicity analysis was performed in a co-culture ratio of 1:5 (cancer cell:T cell) over 24 hours and assessed by LDH release assays in TcE dilution series. We found that BT474 as well as MCF-7 cells were killed effectively with all TcEs, but there was a trend for the effective median concentration (EC_{50}), with A<B=C<D, as well as significant differences in the maximum killing levels, with A>B=C>D (**Fig. 1B & C and Supplementary Figure 1F & G**). Additionally, when measuring the cell-surface levels of early T cell activation markers CD69 and CD25 on BT474 cells, we found that about a 10-fold higher concentration of Format D was required to induce robust upregulation (**Supplementary Figure 1H**). We did not detect any significant differences in the induction of IL-2 and TNFα secretion with 5 pM TcEs in response to $Her2^{high}$ BT474 cells, but MCF-7 cells triggered two-fold more cytokine release in response to Format A than Formats B and C, and no significant cytokine release was elicited by Format D (**Supplementary Figure 2B & C**).

Collectively, these findings demonstrate that while all TcEs can induce cytotoxicity and cytokine release, differences could be detected between formats, particularly at low TAA expression. We set out to investigate the mechanism of these TAA-expression and TcE-format dependent effects.

Initially, we assessed if the different potencies of Formats A-D could be explained by differences in TcE-cell binding. $CD8^+$ T cells, BT747 or MCF-7 cells were stained with 500 pM TcE and each cell type was washed, incubated with fluorescently labelled secondary

antibodies and analyzed by confocal microscopy. We found no major differences in staining intensity for Formats A-D, indicating that there are no practical differences in TcE-cell binding between the formats (**Supplementary Figure 2D-F**). To further evaluate the effect of TAA affinity on TcE mediated cytotoxicity, we tested Formats B-L and C-L for killing of BT747 and MCF-7 cells (**Supplementary Figures 2G & H and 1G**). As expected, the dose response for TcEs with 1000-fold lower TAA affinity was shifted to the right, but maximal killing was identical to Formats B and C, and greater than Format D. Thus, the slightly lower affinity of Format D for Her2 does not account for the superiority of Formats B and C for killing of tumor cells with high or low TAA expression. Next, we assessed whether relative TcE potency might be attributed to differences in their ability to mediate cell-cell adhesion. For this, T cells were fluorescently labelled and added to cancer cell monolayers in the presence of 5 pM TcE. Loosely adherent cells were washed away at different time-points, followed by fixation of the cells and recording of the remaining fluorescence intensity. As the tumor cells express ICAM1, CD58 and CD80 (**Supplementary Figure 2A)**, all of which could contribute to TcE non-specific adhesion (24, 25), we used human serum IgGs as a negative control for TcE-specific effects. T cell-tumor cell adhesion peaked at approximately 2-4 h of co-incubation but no prominent TcE-format-specific differences in cell-cell coupling could be identified for either cancer cell line (**Fig.1D**). Thus, we concluded that the differences in potency between TcE formats is also not based on variations in their ability to mediate cell-cell adhesion. However, when assessing T cell degranulation, a key step in T cell mediated cytotoxicity (26), by staining for cell surface-exposed lysosomal-associated membrane protein 1 (LAMP1) at 21h in cultures with 5 pM TcE and tumor cell targets, we found significantly lower LAMP1 expression with Format D compared to Formats A-C (**Supplementary Figure 3B**). This effect was most pronounced for Her2^{high} BT474 cells. Given our present results, we hypothesized that the distinct TcE potencies for cytotoxicity and other measures of T cell activation might be associated with variations in their ability to generate close membrane-to-membrane proximity.

Induction of efficient and sensitive TCR-signaling at the IS is intricately linked to the size of the extracellular domains of TCR-pMHC and CD2-CD58 complexes and their ability to generate areas of close membrane-to-membrane proximity at ~13 nm that exclude CD45 (27–30). In order to contextualize our TcEs within this framework we performed an in-depth structural analysis, using small-angle X-ray scattering (SAXS) (31), to gain a comprehensive understanding of the physical distances that TcEs can generate between the membrane anchors of CD3ε and the TAA, hereafter referred to as anchor-to-anchor distance. SAXS data were either collected from TcEs alone or from heterotrimers formed between TcEs and the ectodomains of Her2 and CD3εγ. The collected data were analysed by multi-state modelling, resulting in 60-156 states per TcE or heterotrimer, representing the conformational space that

is covered by the respective TcE in solution (**Supplementary Figure 4A & B)**. This was followed by measurements, either of the direct distances between the tips of the antibody-heavy chain CDR3 loops or of the distances between the C-terminal membrane anchorage sites of CD3ε and Her2 for every single state, to obtain paratope- or anchor-to-anchor spacing profiles, respectively (**Fig.2A & Supplementary Figure 5A**). Each individual format alone produced a frequency distribution of paratope-spacings between 5 and 17 nm, with Formats A and B falling into the lower end of this spectrum while Formats C and D where shifted towards larger paratope spacings (**Supplementary Figure 5B)**. However, for anchor-to-anchor spacing of the heterotrimers, the spacing-profile of each individual format became more distinct. Format A had most states at 13 nm (median: 12.7 nm, range: 5-13.9 nm) while Format B had an even shorter median spacing, but a broader distribution of states (median: 11.4 nm, range: 4.2-18.1 nm). Format C had the most states at 18 nm (median: 18.2 nm, range: 12.4-19.5 nm) while Format D exhibited a broader distribution of states with a slightly greater median spacing compared to C (median: 19 nm, range: 7.7-23.4 nm) (**Fig.2B)**. We note that Formats A and B generate distances between the CD3 and Her2 membrane attachment sites that clearly fall within- or below the 13 nm target for physiological membrane apposition (13), while Formats C and D exceed this (**Fig.2B**). A source of variability in anchor-to-anchor distance for TcEs could be flexibility at the hinges and linkers, which can be assessed by SAXS.

In conventional IgG molecules, the flexibility of the two Fab-arms relative to each other, is determined by the number of disulfide bonds in the hinge domain. A higher number of bonds was found to reduce flexibility, leading to fewer conformations and a higher agonistic potential (32) . In the context of our TcEs, Formats A-D are stabilized by two disulfide bonds in the hinge domain, mediated by a CPPC motif. Further, Formats B, C and D exhibit CH1-CL disulfide bonds in the constant region of the their Fab-domains while the single scFv-domains of Formats A, B and D are held together by long flexible linkers (**Fig.2A**). Consequently, we reasoned that our different TcE formats might have different flexibilities that are relevant to our observations. To address this, we qualitatively assessed the degree of disorder/flexibility of our TcEs, either alone or together with bound CD3εγ and Her2, by plotting the SAXS data directly and independently of any modelling as dimensionless Kratky plots (33), where greater flexibility results in a higher amplitude (**Supplementary Figures 6A & B**). Format D exhibited a comparatively high plateau and was well-separated from the other formats under both conditions, indicating a higher degree of flexibility. Interestingly, Format A underwent a strong shift towards lower flexibility upon the addition of antigens. Additionally, we also calculated the maximum particle diameter (D_{max}) and radius of gyration (R_g) values of all states from our multistate modelling approach (**Supplementary Figures 6C & D**). In good agreement with the

modelling-independent Kratky-plots, Format D exhibited the broadest distributions for both parameters, with Formats B & C slightly increasing their range upon addition of antigens while Format A underwent a strong shift towards a smaller range. Taken together, this suggests that Format A is the most constrained and, as a short complex with CD3 and Her2, might be expected to generate an intermembrane spacing of ~13 nm that is consistent with its potent function. However, considering the implications of significant flexibility for the other formats, further data on the actual intermembrane separation that is generated are required, which can only be determined through a previously unexplored quantitative analysis of the TcE-mediated IS.

Initially, we aimed to test the TcEs ability to mediate contact formation in a cell-free system, excluding the contribution of other cell-surface receptor-ligands systems and the repulsive glycocalyx, as well as active cellular processes. To this end, we built a minimal system for membrane-to-membrane contacts where the SLB was functionalized with fluorescently labeled and polyhistidine-tagged recombinant Her2 ectodomains *via* NTA(Ni^{2+}) coupling. Subsequently, we generated giant unilamellar vesicles (GUVs) that we functionalized with CD3$\varepsilon\gamma$ protein, which were then seeded onto the SLB in the presence of soluble TcEs (**Fig.3A**). By combining total internal reflection microscopy (TIRF), together with interference reflection microscopy (IRM) (34), which provides a relative measure for the intermembrane distance at the media-coverslip interface, we were able to systematically evaluate GUV-SLB contact formation by extracting quantitative and structural parameters. When we quantified the IRM signal at sites of Her2 accumulation, where the GUVs were attached to the SLB, we found evidence of close membrane apposition for all formats based on the lower IRM signals obtained versus that in the absence of TcEs (**Fig.3B**). Importantly, the intensity at the contact followed the order A=B=C<D (**Fig.3B & C**). This indicates that the intermembrane separation was similar for contacts mediated by Formats A-C, with a significantly greater intermembrane separation for Format D. It was surprising that Format C generated a similar intermembrane separation as Format A, given that Format C's anchor-to-anchor distance is more similar to Format D in the SAXS data, and Format A's greater potency in functional assays. Assuming that the IRM signal of Format A corresponds to a membrane spacing of ~13 nm, this would require the ~18 nm long complex that is formed by Format C to tilt at a ~45º angle, in order to achieve a similar distance at the GUV-SLB interface.

In the next step, we introduced T cells to the SLB system that we designed to mimic the $Her2^{high}$ and $Her2^{low}$ expression levels on tumor cells. Additionally, we added ICAM1 at 200 molecules/μm^2 to enhance cell attachment (**Fig.3D**). Simultaneous addition of T cells and 5 pM TcEs led to cell adhesion and the rapid formation of synapses, whose temporal dynamics were resolved by fixing the cells at different time-points post-addition to the SLB, followed by

staining for F-actin. TcE localization was visualized by staining with fluorescently labelled anti-Fc-domain secondary antibodies. Qualitative inspection of the data revealed striking similarities of TcE-formed adhesion sites to synapses previously observed in natural cell-cell and SLB systems(35). Within 15 min post-attachment, adhesion sites with bulls-eye concentric actin structures, reminiscent of dSMACs, were frequently observed (**Figure 3E**). In the center of these structures, we found accumulation of Her2, which is similar to the localization of the TCR-pMHC pair in the natural monofocal IS. This cSMAC-like region was also where strong anti-TcE staining was detected, indicating successful TcE-based linkage of Her2 and CD3ε within the IS. We further verified this correlation by measuring colocalization of the anti-TcE signal and Her2 *via* one-to-one pixel matching (**Supplementary Figure 7A & B**). Importantly, these structures were completely absent in negative-control samples, incubated with non-specific human serum IgG in place of the TcE, with overall fewer cellular attachments. However, in contrast to natural- or anti-TCR antibody-mediated monofocal synapses, where ICAM1-LFA-1 interactions are observed mostly within a ring-like arrangement in the pSMAC region and excluded from the cSMAC (**Supplementary Figure 7C**), we found predominantly diffusive and central accumulation of ICAM1 in TcE-mediated adhesions (**Fig.3E**). Immunostaining for ICAM1 in $CD8^+$ T cell and cancer cell co-cultures aligned with this observation, with ICAM1 being enriched but evenly distributed within the cell-cell contact site (**Supplementary Figure 7D**). Her2 and TcE-enriched contacts were also observed for the higher TcE concentration of 500 pM, although adhesion sites were observed less frequently under these conditions, potentially due to saturated TcE binding of Her2 and CD3ε (**Supplementary Figure 8A**). TcE concentrations of 0.5 pM did not elicit adhesion of the T cells to the substrate. In addition to the monofocal configuration, we also observed a second phenotype that lacked concentric actin patterns and featured speckled puncta of Her2, anti-TcE and ICAM1 within the cell contact site (**Supplementary Figure 8B**).

In order to quantitatively resolve how the different TcE formats impact on the dynamics of IS formation, we assessed the formation frequency of monofocal IS-like adhesion sites over time. For this, we implemented an automated detection of monofocal actin structures into our analysis pipeline *via* a global, histogram-based, segmentation of cell-contact areas, coupled to image erosion and measurement of the Hessian matrix eigenvalues of the F-actin staining (**Supplementary Figure 9**). This allowed for automated detection of bulls-eye structures, indicative of mature monofocal IS formation as well as their discrimination against other adhesive contact sites. We found that bulls-eye structures were most frequent among contact sites between 5-15 min of incubation on $Her2^{high}$ SLBs. This was slightly shifted towards a maximum after 10-25 min of incubation for $Her2^{low}$ SLBs. Under both conditions, bulls-eye structures were mostly disassembled and cells detached from the SLBs after 60 min (**Fig.3F**).

Remarkably, there were striking differences in IS frequency and dynamics between TcE formats following the trend A=B=C>D. While Formats A-C formed bulls-eye structures with an average frequency of 41% of total adhesion sites over all time points, T cells incubated with Format D only reached an average frequency of 27%. Moreover, Formats A-C produced IS-like adhesions earlier and over longer time periods compared to Format D, highlighting differences in the temporal dynamics of IS formation among the different TcE architectures (**Fig.3F**). In this context, the frequency of mature, monofocal IS formation has been associated with the potency of immunotherapies and immune evasion in the tumor microenvironment (36, 37).

Next, we decided to analyze the IRM signatures of the entire IS formed by $CD8^+$ T cells on the SLBs. Unlike the cell-free GUV-SLB system, these measurements not only depend upon TcE-mediated close membrane apposition, but integrate LFA-1-ICAM1 dependent adhesion, and the repulsive effect of the cellular glycocalyx. Addition of T cells to the SLBs resulted in the rapid formation of large contact areas that remained relatively stable over the 40-minute period of observation and we could not find any pronounced differences in the area of the contact between the different TcE-formats (**Supplementary Figure 8C)**. However, the IRM data showed significant variation across conditions with Formats A & B exhibiting the lowest IRM intensities within the first 15 min of contact, followed by Format C, which in turn was well separated from Format D (**Fig.4A**). At 25 min, Format D continued to exhibit the highest IRM intensity whereas Formats A-C converged around a similar value. This was followed by a general increase of IRM-intensities at 40 min, indicative of beginning cell detachment (**Fig.4A**). Overall, these effects were less pronounced for $Her2^{low}$ conditions, with higher fluctuations in IRM intensities from time-point to time-point, perhaps due to the greater role of other, non-TcE factors that determine the IRM signal at the IS. Nevertheless, Formats A-C still tended to exhibit lower IRM intensities than Format D (**Fig.4A**). When we used the low-Her2 affinity TcE Formats B-L and C-L and quantified the IRM signal, there was only a modest increase in brightness compared to their parent constructs, perhaps due to a greater relative contribution of LFA-1-ICAM1 to the IS distance, while Format D still exhibited the greatest IRM intensity of all tested TcEs (**Supplementary Figure 10A)**. We thus concluded that the comparatively small differences in affinity for Her2 between Formats A-D are negligible and the inability of Format D to create close membrane apposition is not due to lower affinity. Taken together, and in agreement with the measurements from SAXS, Formats A & B generated consistently close membrane appositions, followed by Format C and then, distantly, Format D.

Next, we made use of a recently established method to directly test the TcEs ability to mediate the exclusion of proteins with large ECDs from the IS (38). The method uses the fluorescently labelled ectodomain of CD45RABC, which is efficiently excluded from close-contacts (39) and

that is expressed by cells in the B-cell lineage (40), making it relevant as all approved TcEs are directed at cancers of this origin. Addition of this 'exclusion probe' to the SLB produced a homogenous fluorescence signal. However, contacts made by cells were marked by the local depletion of fluorescence, produced by the exclusion of the probe from the regions of contact, but only if the cell-SLB contact was sufficiently close (<15 nm(30); **Fig.4B & C**). As expected, and consistent with SAXS-measurements (**Fig. 2B**), Format D displayed minimal probe exclusion, supporting the notion that it creates a membrane-to-membrane distance that is too large to efficiently exclude proteins with large ECDs. Importantly, Format C, predicted by SAXS to have a similar mean distance between membrane anchors as Format D, excluded the probe as effectively as Formats A and B. Notably, we occasionally observed accumulation of the CD45-based exclusion probe at the center of the IS (**Supplementary Figure 10B**), resulting in some negative values for probe exclusion (Fig.4B). This was potentially attributable to glycocalyx interactions mediated by T cell-expressed galectins (41) or sialoadhesins (42). However, these events were noted across all formats and did not influence the relative outcome of the comparison between TcEs.

We next turned to the analysis of signaling at the IS to determine if we could identify parameters that better explain the different functional potencies of the different formats. TcE potency at the IS can be evaluated by fixing T cells during IS formation (~20 min) on SLBs and staining with antibodies against signaling components, such as the phosphorylated form of Zeta-chain-associated protein kinase 70 (pZap-70). pZap-70 staining followed the trend A>B=C>D, especially at high densities of Her2 (**Fig.5A & B**), which aligned better with cytotoxic potency. Next, we asked if our ability to distinguish the different TcEs could be improved by considering the role of co-stimulation.

To this end, we added CD58, the ligand for co-stimulatory receptor CD2 on T cells, to Her2 and ICAM1 SLBs. CD2-CD58 spans a distance of ~13 nm and provides a potent co-stimulatory signal that synergizes with the TCR in the phosphorylation of Phospholipase Cγ1 (pPLCγ1) (9, 43). The ability to cooperate with the CD2-CD58 interaction has recently been highlighted as an important parameter for chimeric antigen receptors (44). Thus, we hypothesized that the ability to cooperate with CD2-CD58 interactions will also be important for TcEs. Addition of CD58 to the SLB under $Her2^{high}$ conditions led to a marked increase in pPLCγ1 staining compared to the control situation with Her2 and ICAM1 alone, with the effect following the order A>B>C, while there was no significant effect with Format D (**Fig.5C & D**). Importantly, this was also correlated with the levels of CD58 recruitment to the IS with the order A>B>C=D (**Fig.5D & E**). These effects were similar under $Her2^{low}$ conditions although they were only significant for Format A (**Fig.5C & D**). These data support the hypothesis that TcEs can be ranked based on recruitment of CD2-CD58.

Discussion

Taken together, we have found that combining SAXS with bilayer-bilayer interface and IS measurements is a powerful approach to understand TcE mechanisms that account for the observed potency in tumor killing (**Supplementary Figure 10C**). Format A generates soluble complexes with 13 nm anchor-to-anchor spacing and membrane-to-membrane distances and IS characteristics that support ≤ 13 nm membrane separation across conditions. Format A is closest to a natural TCR-pMHC interaction and, correspondingly, is the most potent format in killing tumor targets at $Her2^{high}$ and $Her2^{low}$ expression levels. Format B had greater flexibility, with a wide spread of anchor-to-anchor distances around 13 nm in solution and is distinguished from Format A by its lower efficiency in recruiting CD2-CD58 interactions. Format C exhibited no states that would fit with SAXS data closer than an anchor-to-anchor spacing of 15 nm, with the majority of states at 18 nm. Surprisingly, the bilayer-bilayer interface and IS data for Format C were similar to Formats A and B, except that it was even less efficient than B at recruiting CD2-CD58 interactions. Thus, for both Formats B and C, their intermediate potency is best accounted for by failure to optimally recruit co-stimulation, which is the most stringent test for optimal TcE potency. Finally, Format D, with its flexible C-terminal modification of the Fc-domain, retained the ability to mediate adhesion between T cells and tumor cells, but generated more distant contacts by both bilayer-bilayer interface and IS measurements; it failed to exclude CD45 or to recruit CD2-CD58 interactions.

Our study thus presents a first, in-depth systematic assessment of the structure-to-function relationship of TcEs to IS formation. By combining cellular assays, structural measurements by SAXS, and a controlled, reductionist SLB-based approach, we identify a sequence of steps that increase potency as they are completed: 1.) mediate cell-cell adhesion, 2.) exclude large, inhibitory ECDs like CD45, and 3.) promote co-stimulatory receptor/ligand interactions. While we could not detect any differences between the tested TcEs for 1, suggesting that cell-cell adhesion is primarily determined by antigen affinity, we find that TcE-architecture impacts on 2 and 3 by setting the membrane-to-membrane distance at the IS, which in turn governs T cell signaling and the temporal dynamics of IS formation and durability (**Supplementary Figure 10D**).

We find that there is a complex relationship between paratope-spacing derived from simple, linear models of TcEs and actual 3D-distributions derived from structural measurements. Importantly, paratope-spacing does not necessarily correspond to the spacing observed between antigens in complexes with TcEs. Furthermore, this spacing alone is not entirely predictive of their potency to mediate close membrane apposition at the IS where other factors such as bending and tilting have to be considered.

Our results suggest that the linear distance between membrane attachment sites derived from SAXS is not the same as the intermembrane separation that would impact on local CD45 exclusion and co-localization with co-stimulatory receptor-ligand pairs. While small (~14 nm) adhesion proteins like CD2-CD58 (45) form complexes that are nearly fully extended at the physiological intermembrane separation of 13 nm, longer molecules undergo tilting at the interface. For instance, LFA-1-ICAM1 interactions, with a nominal length of 50 nm are able to generate sufficiently close intermembrane spacing to partly exclude CD45 (38, 46) due to tilting, which is promoted by tangential cytoskeletal forces (47). Furthermore, it has been shown for CD48, another CD2-ligand, that addition of Ig-like domains adds 4 nm per domain to the extended length of the protein, but only leads to a 1 nm per Ig-like domain increase in intermembrane separation (12), indicating significant "tilting" or longer intermembrane complexes. Format D is a tandem array with 5 Ig-like domains, similar to extending Format A by 3 Ig-like domains. Prior studies suggest that each Ig-like domain generates 1 nm increase in intermembrane spacing leading to an intermembrane separation of ~16 nm, which is larger than the rigid globular core of the CD45 ECD at ~15.2 nm (30) (**Supplementary Figure 10C**). Formats C and D have significant overlap in anchor-to-anchor separation, but we speculate that the Y- shaped Format C and the absence of additional linkers in the hinges may enable this format to favor the necessary tilting (~45°) to allow CD45 exclusion (**Supplementary Figure 10C**).

Interestingly, the differences between Formats A, B and C could not be resolved in the bilayer-bilayer interface measurements where the IRM signals for Format A-C are indistinguishable from each other. Potentially, this is due to the absence of a negatively charged glycocalyx (48) in the bilayer-bilayer interface system. Glycocalyx repulsion, combined with the capacity of Format B and C to accommodate greater spacing, through conformational states or variable tilting angles, might account for the failure of Formats B and C to generate the optimal intermembrane spacing for CD2-CD58 interaction. On the other hand, Format A is fully extended at 13 nm, similar to the CD2-CD58 interaction. In contrast to Formats A-C, Format D showed a significantly larger membrane-to-membrane distance, limited exclusion of large ECDs and very reduced engagement of CD2-CD58 (**Supplementary Figure 10C**). Despite its limitations, Format D mediated efficient killing with Her2^{high} targets. This can be explained by the high affinity of the engager and the notion that a high density of TCR ligands can overcome the suppressive effect of insufficient CD45 exclusion by packing engaged TCRs at < 50 nm lateral spacing (14). This may be a desirable feature when designing TcEs against TAAs that are expressed broadly, but at higher levels in tumors than other tissues.

Importantly, our findings have significant implications for understanding the function of many already existing, clinically approved TcEs and some in clinical trials. Blinatumomab, the first

approved TcE, targets CD19 and its structure (49) suggests that the CD3ε-Blinatumomab-CD19 complex would create a complex small enough to exclude CD45, though its relationship to CD2-CD58 would need to be empirically determined. All the other approved TcEs target CD20, which like the trastuzumab binding to Her2, is a membrane proximal epitope (50). Approved drugs Epcoritamab (51), Mosunetuzamab (52) or Odronextamab (53) are Format C-like and close membrane apposition would likely depend upon tilting of the complex. Plamotamab (54) is a Format B-like TcE, which we would predict to perform equally or slightly better than Format C. Glofitamab on the other hand is Format C-like, but has an additional anti-CD20 paratope linked to the Fab arm bearing the anti-CD3 (55). The additional anti-CD20 may further stabilize the tilted configuration and might boost target killing by establishing a stable platform for CD2-CD58 recruitment. However, it would be important to determine which, if any of these effective drugs take full advantage of CD2-CD58 or other co-stimulatory pairs like CD28-CD80. Further experiments will be required to verify if the ability of Format C to promote tilting can be translated to other membrane proximal epitopes and if this tilting strategy to generate close contacts can be reliably predicted by SLB experiments with either cells or GUVs, which will make this an invaluable addition to the early characterization of new TcE designs.

Notably, the role of CD2-CD58 interactions differs in the context of high-affinity TcEs compared to their likely contribution at physiological synapses. According to the KS model, CD2-CD58 is thought to lower activation thresholds by facilitating the formation of small initial close contacts, allowing the physiological TCR scanning of pMHC (11), as has been observed (38). However, in the case of high affinity TcEs, which bind orders of magnitude faster than CD2 to CD58, the membrane-to-membrane distance appears to be first determined by the TcE, which can allow or prevent CD2-CD58 interactions, subsequently influencing downstream signaling.

Regarding potential limitations, the SAXS data are limited by the complexity of data fitting for flexible proteins. However, our interpretation that the Format C-antigen complex must tilt in the interface is also consistent with models for IgG conformational states with an average angle between IgG1 Fab arms of 120° (56). While the SLB system allowed us to resolve the structure and dynamics of the self-assembled membrane-membrane interfaces and TcE-mediated IS in unprecedented detail, it has to be acknowledged that it does not fully recapitulate the active participation (e.g. F-actin based transport and ligand immobilization) and potential biophysical cues (e.g. membrane topology) of the target cell. Further, while our SLB system does mirror Her2 densities found on target cells, it does not fully recapitulate all (co-) stimulatory signals and glycocalyx components that are expressed on target cells. However, it has been shown that IS function and architecture in SLBs are well correlated with

natural synapses formed at cell-cell contacts and therefore represents a realistic model system (57). We also note that our TAA-SLB system can be easily adapted to present additional co-stimulatory ligands and other components of the glycocalyx (38), making it a potentially valuable tool to study the efficiency of different TcE designs against a variety of surrogate cell-surface compositions.

In summary, we have defined a pipeline for TcE analysis based on testing cell-cell adhesion, solution interaction by SAXS, and SLB-based bilayer-bilayer interface and IS assays that enable effective prediction and interpretation of TcE-performance. Our data support a sequence of events required for TcE function based on 1.) adhesion, 2.) CD45 exclusion, and 3.) CD2-CD58 recruitment. The potency of TcEs that achieve step 1, but not 2 and 3 is low as high TAA-densities are required to closely space TCRs for triggering in the absence of CD45 exclusion. Moving forward, we propose that considerations of these mechanisms will be instrumental in the design of future TcE formats, enabling precise tuning of their performance, based on tissue- and tumor-specific levels of TAA expression.

Acknowledgments and funding sources: Kennedy Trust for Rheumatology Research and Boehringer Ingelheim Pharmaceuticals. O.S. acknowledges support from the Joachim Herz foundation (Add-on fellowship). A.L. is funded by an Erwin Schrödinger postdoctoral fellowship of the Austrian Science Fund (FWF, project number: J4542-B) and is an EMBO non-stipendiary postdoctoral fellow (ALTF 1109-2020). We would like to thank the antibody expression and purification (APEX) team at Boehringer Ingelheim for providing high quality material to support this study. The authors thank Claire Pizzey and her dedicated team at the synchrotron beamline B21 at Diamond Light Source (Oxford, UK) for their organization and execution of the SAXS measurements, as well as their valuable advisory support.

References:

1. A. D. Waldman, J. M. Fritz, M. J. Lenardo, A guide to cancer immunotherapy: from T cell basic science to clinical practice. *Nat Rev Immunol* **20**, 651–668 (2020).

2. A. Trabolsi, A. Arumov, J. H. Schatz, T Cell-Activating Bispecific Antibodies in Cancer Therapy. *J Immunol* **203**, 585–592 (2019).

3. U. Brinkmann, R. E. Kontermann, The making of bispecific antibodies. *MAbs* **9**, 182–212 (2017).

4. P. Roda-Navarro, L. Álvarez-Vallina, Understanding the Spatial Topology of Artificial Immunological Synapses Assembled in T Cell-Redirecting Strategies: A Major Issue in Cancer Immunotherapy. *Front Cell Dev Biol* **7**, 370 (2019).

5. S. Dickopf, G. J. Georges, U. Brinkmann, Format and geometries matter: Structure-based design defines the functionality of bispecific antibodies. *Comput Struct Biotechnol J* **18**, 1221–1227 (2020).

6. B. H. Santich, *et al.*, Interdomain spacing and spatial configuration drive the potency of IgG-[L]-scFv T cell bispecific antibodies. *Sci Transl Med* **12**, 1–11 (2020).

7. U. Wuellner, *et al.*, Bispecific CD3/HER2 Targeting FynomAb Induces Redirected T Cell-Mediated Cytolysis with High Potency and Enhanced Tumor Selectivity. *Antibodies* **4**, 426–440 (2015).

8. J. B. Huppa, M. M. Davis, T-cell-antigen recognition and the immunological synapse. *Nat Rev Immunol* **3**, 973–83 (2003).

9. P. Demetriou, *et al.*, A dynamic CD2-rich compartment at the outer edge of the immunological synapse boosts and integrates signals. *Nat Immunol* **21**, 1232–1243 (2020).

10. S. Offner, R. Hofmeister, A. Romaniuk, P. Kufer, P. A. Baeuerle, Induction of regular cytolytic T cell synapses by bispecific single-chain antibody constructs on MHC class I-negative tumor cells. *Mol Immunol* **43**, 763–771 (2006).

11. S. J. Davis, P. A. van der Merwe, The kinetic-segregation model: TCR triggering and beyond. *Nat Immunol* **7**, 803–9 (2006).

12. O. Milstein, *et al.*, Nanoscale increases in CD2-CD48-mediated intermembrane spacing decrease adhesion and reorganize the immunological synapse. *Journal of Biological Chemistry* **283**, 34414–34422 (2008).

13. K. Choudhuri, D. Wiseman, M. H. Brown, K. Gould, P. A. van der Merwe, T-cell receptor triggering is critically dependent on the dimensions of its peptide-MHC ligand. *Nature* **436**, 578–82 (2005).

14. H. Cai, *et al.*, Full control of ligand positioning reveals spatial thresholds for T cell receptor triggering. *Nat Nanotechnol* **13**, 610–617 (2018).

15. J. Li, *et al.*, Membrane-Proximal Epitope Facilitates Efficient T Cell Synapse Formation by Anti-FcRH5/CD3 and Is a Requirement for Myeloma Cell Killing. *Cancer Cell* **31**, 383–395 (2017).

16. C. Bluemel, *et al.*, Epitope distance to the target cell membrane and antigen size determine the potency of T cell-mediated lysis by BiTE antibodies specific for a large melanoma surface antigen. *Cancer Immunology, Immunotherapy* **59**, 1197–1209 (2010).

17. M. L. Dustin, "Insights into Function of the Immunological Synapse from Studies with Supported Planar Bilayers" in *Current Topics in Microbiology and Immunology*, (2010), pp. 1–24.

18. S. Sandin, L.-G. Ofverstedt, A.-C. Wikström, O. Wrange, U. Skoglund, Structure and flexibility of individual immunoglobulin G molecules in solution. *Structure* **12**, 409–15 (2004).

19. S. Venkataramani, *et al.*, Design and characterization of Zweimab and Doppelmab, high affinity dual antagonistic anti-TSLP/IL13 bispecific antibodies. *Biochem Biophys Res Commun* **504**, 19–24 (2018).

20. K. M. Ferguson, Structure-based view of epidermal growth factor receptor regulation. *Annu Rev Biophys* **37**, 353–373 (2008).

21. S. Pessano, H. Oettgent, A. K. Bhan, The T3/T cell receptor complex: antigenic distinction between the two 20-kd T3 (T3-6 and T3-E) subunits. **4**, 337–344 (1985).

22. J. Middelburg, *et al.*, Overcoming Challenges for CD3-Bispecific Antibody Therapy in Solid Tumors. *Cancers (Basel)* **13** (2021).

23. S. Boero, *et al.*, Analysis of in vitro ADCC and clinical response to trastuzumab: possible relevance of FcγRIIIA/FcγRIIA gene polymorphisms and HER-2 expression levels on breast cancer cell lines. *J Transl Med* **13**, 324 (2015).

24. A. Kupfer, S. J. Singer, The specific interaction of helper T cells and antigen-presenting B cells. IV. Membrane and cytoskeletal reorganizations in the bound T cell as a function of antigen dose. *J Exp Med* **170**, 1697–713 (1989).

25. K. Somersalo, *et al.*, Cytotoxic T lymphocytes form an antigen-independent ring junction. *J Clin Invest* **113**, 49–57 (2004).

26. D. T. Shen, J. S. Y. Ma, J. Mather, S. Vukmanovic, S. Radoja, Activation of primary T lymphocytes results in lysosome development and polarized granule exocytosis in CD4+ and CD8+ subsets, whereas expression of lytic molecules confers cytotoxicity to CD8+ T cells. *J Leukoc Biol* **80**, 827–37 (2006).

27. P. A. van der Merwe, O. Dushek, Mechanisms for T cell receptor triggering. *Nat Rev Immunol* **11**, 47–55 (2011).

28. T. A. Springer, Adhesion receptors of the immune system. *Nature* **346**, 425–34 (1990).

29. J. R. James, R. D. Vale, Biophysical mechanism of T-cell receptor triggering in a reconstituted system. *Nature* **487**, 64–69 (2012).

30. V. T. Chang, *et al.*, Initiation of T cell signaling by CD45 segregation at "close contacts." *Nat Immunol* **17**, 574–582 (2016).

31. L. Boldon, F. Laliberte, L. Liu, Review of the fundamental theories behind small angle X-ray scattering, molecular dynamics simulations, and relevant integrated application. *Nano Rev* **6**, 25661 (2015).

32. C. M. Orr, *et al.*, Hinge disulfides in human IgG2 CD40 antibodies modulate receptor signaling by regulation of conformation and flexibility. *Sci Immunol* **7**, eabm3723 (2022).

33. A. G. Kikhney, D. I. Svergun, A practical guide to small angle X-ray scattering (SAXS) of flexible and intrinsically disordered proteins. *FEBS Lett* **589**, 2570–2577 (2015).

34. H. Verschueren, Interference reflection microscopy in cell biology: methodology and applications. *J Cell Sci* **75**, 279–301 (1985).

35. M. L. Dustin, The immunological synapse. *Cancer Immunol Res* **2**, 1023–33 (2014).

36. L. R. Díaz, *et al.*, Imbalance of immunological synapse-kinapse states reflects tumor escape to immunity in glioblastoma. *JCI Insight* **3** (2018).

37. W. Xiong, *et al.*, Immunological Synapse Predicts Effectiveness of Chimeric Antigen Receptor Cells. *Mol Ther* **26**, 963–975 (2018).

38. E. Jenkins, *et al.*, Antigen discrimination by T cells relies on size-constrained microvillar contact (2023) https:/doi.org/10.1038/s41467-023-36855-9.

39. C. B. Carbone, *et al.*, In vitro reconstitution of T cell receptor-mediated segregation of the CD45 phosphatase. *Proc Natl Acad Sci U S A* **114**, E9338–E9345 (2017).

40. M. L. Hermiston, Z. Xu, A. Weiss, CD45: A critical regulator of signaling thresholds in immune cells. *Annu Rev Immunol* **21**, 107–137 (2003).

41. K. E. Pace, C. Lee, P. L. Stewart, L. G. Baum, Restricted receptor segregation into membrane microdomains occurs on human T cells during apoptosis induced by galectin-1. *J Immunol* **163**, 3801–11 (1999).

42. A. Vuchkovska, *et al.*, Siglec-5 is an inhibitory immune checkpoint molecule for human T cells. *Immunology* **166**, 238–248 (2022).

43. N. Espagnolle, *et al.*, CD2 and TCR synergize for the activation of phospholipase Cγ1/calcium pathway at the immunological synapse. *Int Immunol* **19**, 239–248 (2007).

44. J. Burton, *et al.*, Inefficient exploitation of accessory receptors reduces the sensitivity of chimeric antigen receptors. *Proceedings of the National Academy of Sciences* **120** (2023).

45. J. H. Wang, *et al.*, Structure of a heterophilic adhesion complex between the human CD2 and CD58 (LFA-3) counterreceptors. *Cell* **97**, 791–803 (1999).

46. S. A. Freeman, *et al.*, Integrins Form an Expanding Diffusional Barrier that Coordinates Phagocytosis. *Cell* **164**, 128–140 (2016).

47. P. Nordenfelt, *et al.*, Direction of actin flow dictates integrin LFA-1 orientation during leukocyte migration. *Nat Commun* **8** (2017).

48. S. Maschalidi, K. S. Ravichandran, Phagocytosis: Sweet Repulsions via the Glycocalyx. *Current Biology* **31**, R20–R22 (2021).

49. A. Teplyakov, G. Obmolova, J. Luo, G. L. Gilliland, Crystal structure of B-cell co-receptor CD19 in complex with antibody B43 reveals an unexpected fold. *Proteins* **86**, 495–500 (2018).

50. L. Rougé, *et al.*, Structure of CD20 in complex with the therapeutic monoclonal antibody rituximab. *Science* **367**, 1224–1230 (2020).

51. H. J. van der Horst, *et al.*, Epcoritamab induces potent anti-tumor activity against malignant B-cells from patients with DLBCL, FL and MCL, irrespective of prior CD20 monoclonal antibody treatment. *Blood Cancer J* **11**, 38 (2021).

52. L. L. Sun, *et al.*, Anti-CD20/CD3 T cell-dependent bispecific antibody for the treatment of B cell malignancies. *Sci Transl Med* **7** (2015).

53. R. Bannerji, *et al.*, Odronextamab, a human CD20×CD3 bispecific antibody in patients with CD20-positive B-cell malignancies (ELM-1): results from the relapsed or refractory non-Hodgkin lymphoma cohort in a single-arm, multicentre, phase 1 trial. *Lancet Haematol* **9**, e327–e339 (2022).

54. K. Patel, *et al.*, A Phase 1 Study of Plamotamab, an Anti-CD20 x Anti-CD3 Bispecific Antibody, in Patients with Relapsed/Refractory Non-Hodgkin's Lymphoma: Recommended Dose Safety/Efficacy Update and Escalation Exposure-Response Analysis. *Blood* **140**, 9470–9472 (2022).

55. M. Bacac, *et al.*, CD20-TCB with Obinutuzumab Pretreatment as Next-Generation Treatment of Hematologic Malignancies. *Clin Cancer Res* **24**, 4785–4797 (2018).

56. X. Zhang, *et al.*, 3D Structural Fluctuation of IgG1 Antibody Revealed by Individual Particle Electron Tomography. *Sci Rep* **5**, 9803 (2015).

57. M. L. Dustin, Supported bilayers at the vanguard of immune cell activation studies. *J Struct Biol* **168**, 152–60 (2009).

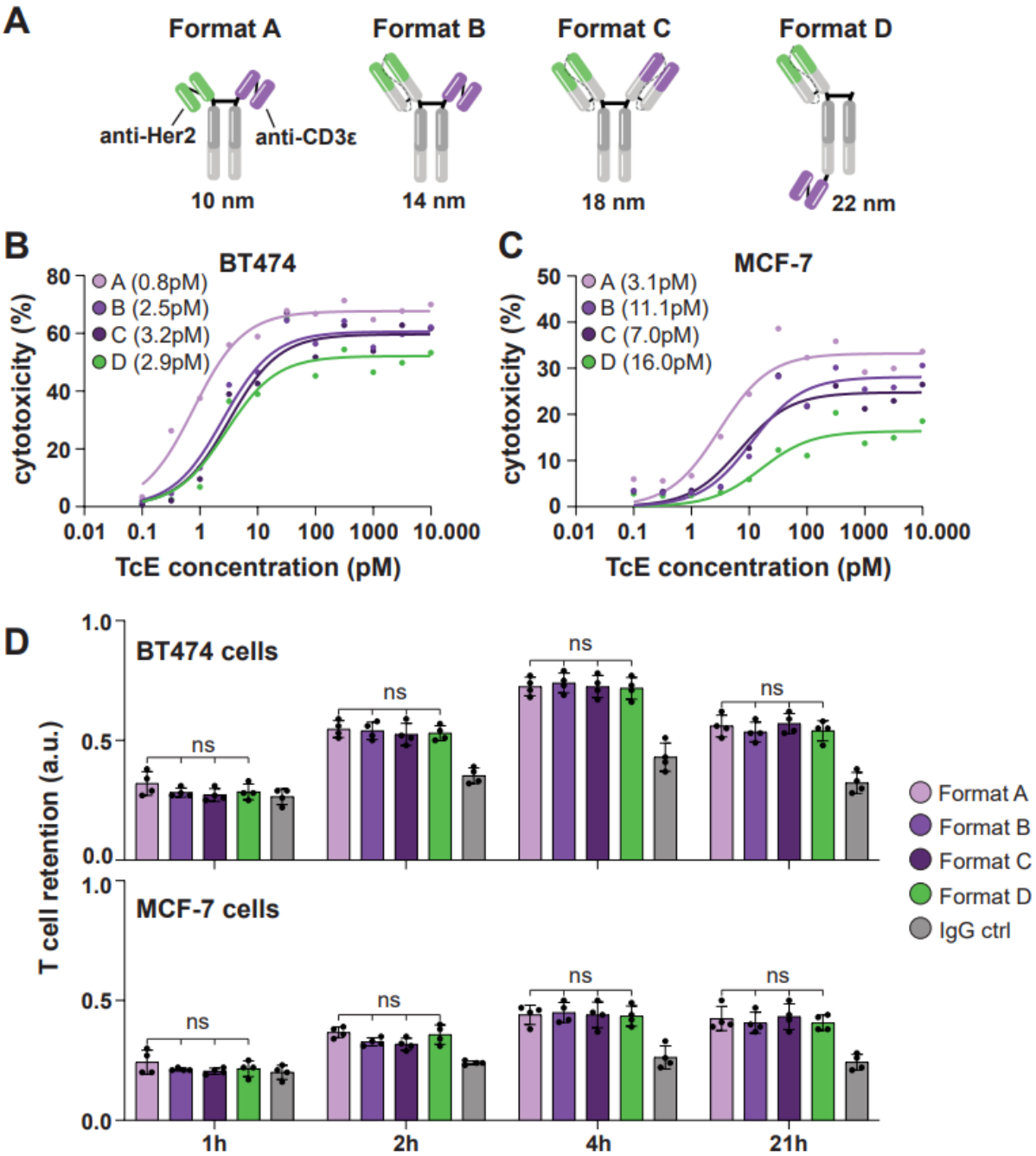

Figure 1. **Structure and functional analysis of TcEs.** (**A**) Schematic overview of TcE formats. (**B**) BT474 or MCF-7 (**C**) tumour cell cytotoxicity upon increasing TcE concentrations after 24h of co-incubation in a tumour cell: T cell ratio of 1:5. Single data points represent the median of 3 biological replicates. Lines represent the non-linear fit of the data. (**D**) Time-series of the relative retention of T cells on BT474 (top) or MCF-7 (bottom) tumour cells in the presence of TcEs or IgG control. Mean ± SD, 2 biological replicates, 2way ANOVA, ns=not significant.

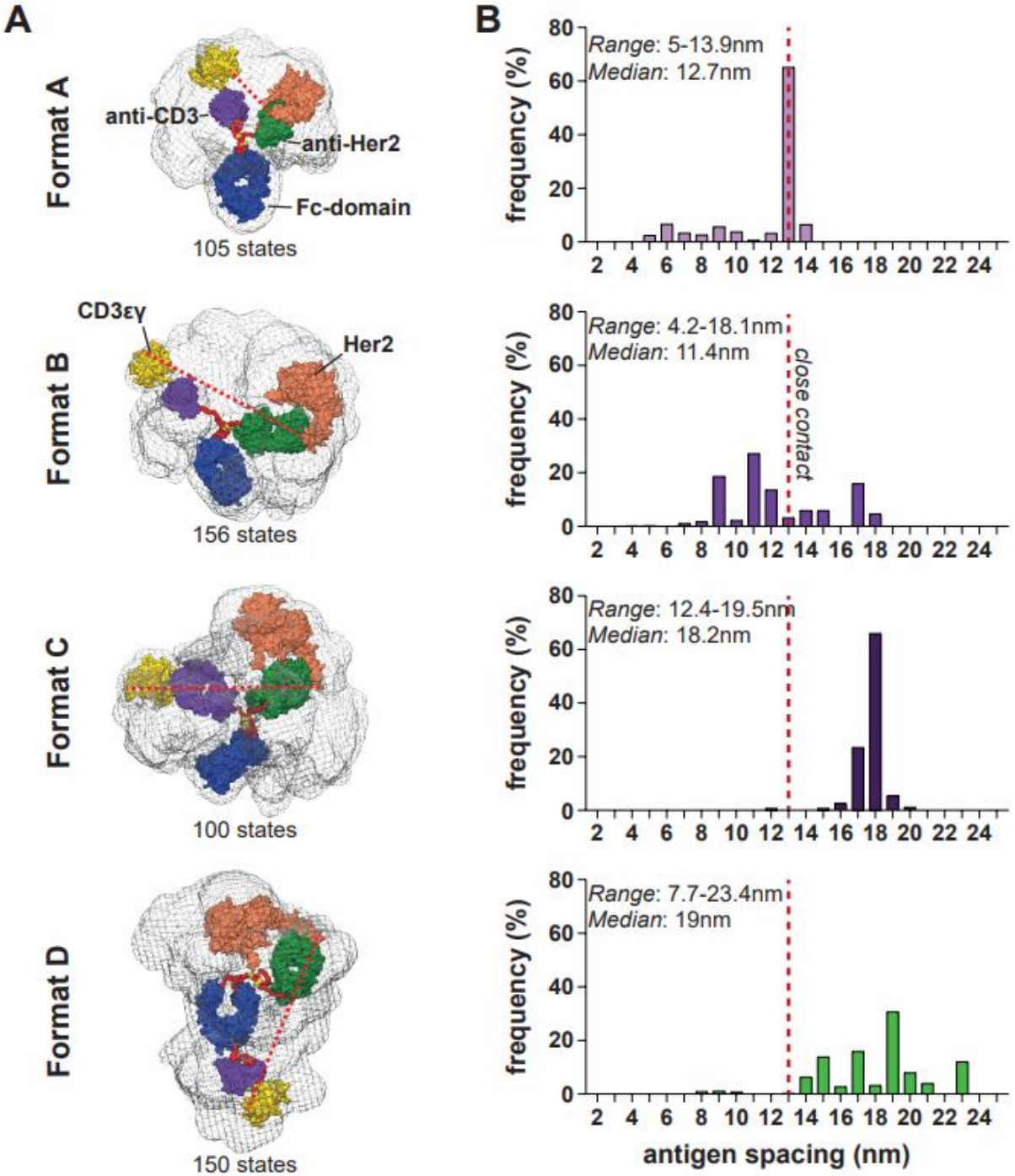

Figure 2. **SAXS-derived conformational space and antigen-spacing.** (**A**) Conformational space of TcE-antigen complexes in solution. Grey meshes show overlay of all conformational states of each molecule. One single state per molecule is shown as coloured surface representation. Magenta = anti-CD3, green = anti-Her2, blue = F_c-domain, yellow = CD3εγ, salmon = Her2. Flexible residues are shown in red. Disulphide bonds in the hinge region are shown in yellow. Dashed red line illustrates measurement of the distance between antigens. (**B**) SAXS-data derived frequency distributions of antigen-spacings. Red dashed lines indicate close contact zone at 13nm.

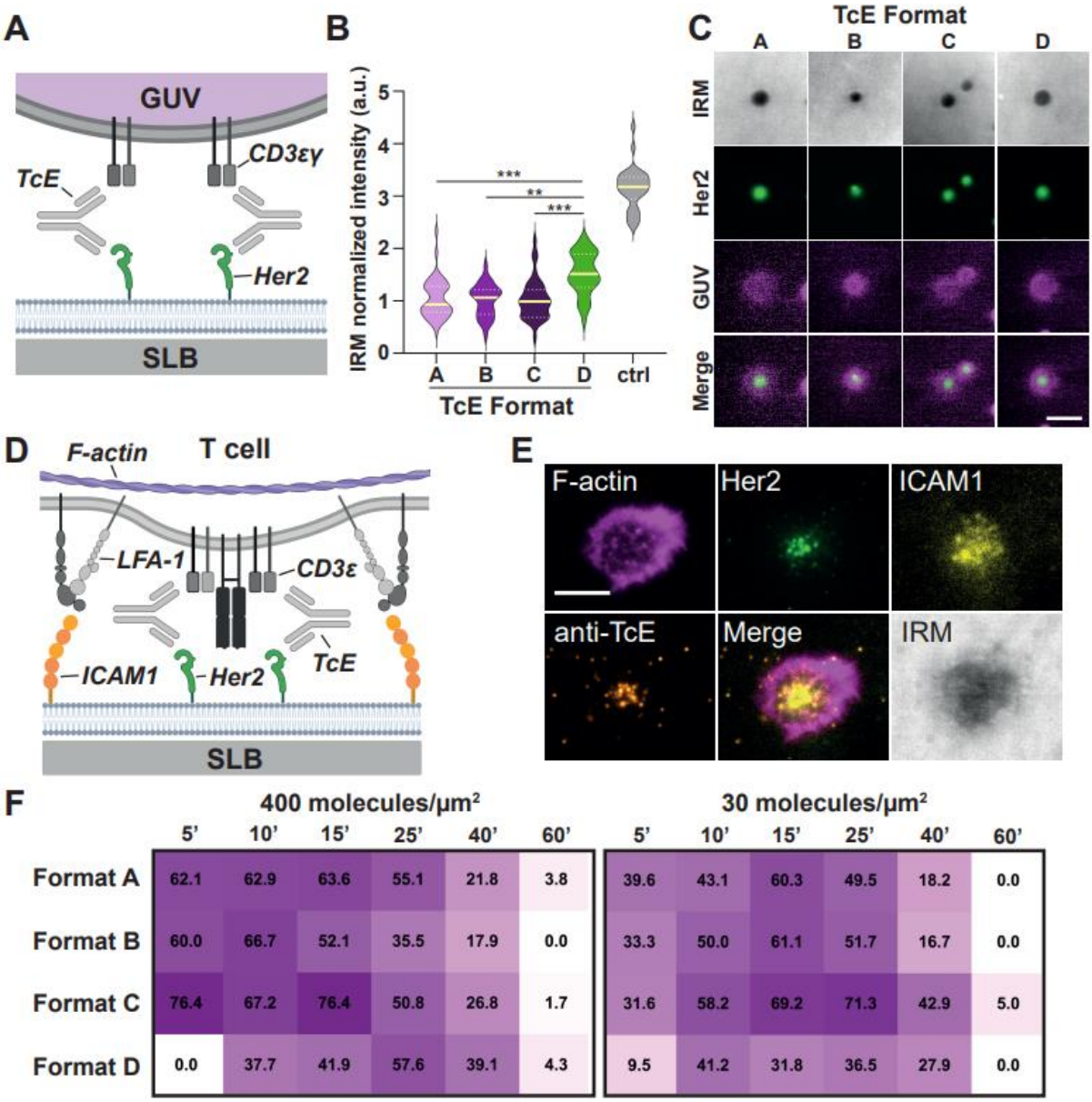

F

	400 molecules/µm²						30 molecules/µm²					
	5'	10'	15'	25'	40'	60'	5'	10'	15'	25'	40'	60'
Format A	62.1	62.9	63.6	55.1	21.8	3.8	39.6	43.1	60.3	49.5	18.2	0.0
Format B	60.0	66.7	52.1	35.5	17.9	0.0	33.3	50.0	61.1	51.7	16.7	0.0
Format C	76.4	67.2	76.4	50.8	26.8	1.7	31.6	58.2	69.2	71.3	42.9	5.0
Format D	0.0	37.7	41.9	57.6	39.1	4.3	9.5	41.2	31.8	36.5	27.9	0.0

Figure 3. **TcE-mediated GUV- and T cell-SLB IS formation.** (**A**) Schematic overview of GUV-SLB experimental system. (**B**) Normalized IRM intensities at the TcE-mediated IS between Her2-containing SLBs and GUVs. Yellow solid line = median, White dashed line = quartiles. 2 biological replicates, Kruskal-Wallis test, ** $p<0.005$, *** $p<0.0005$. (**C**) Representative TIRF, IRM and brightfield images of TcE mediated IS formation between Her2-containing (green) SLBs and functionalized GUVs (magenta). Scale bars = 5µm. (**D**) Schematic overview of T cell-SLB experimental system. (**E**) Representative TIRF and IRM images of TcE-mediated IS formation on SLB after 25min. of incubation, scale bar = 6µm. (**F**) Time-resolved analysis of TcE-mediated immune synapse formation frequency of T cells on SLBs. Numbers in the boxes represent the percentage of cell-adhesion sites with bulls-eye actin structures. Numbers on top indicate time in minutes. 2 biological replicates.

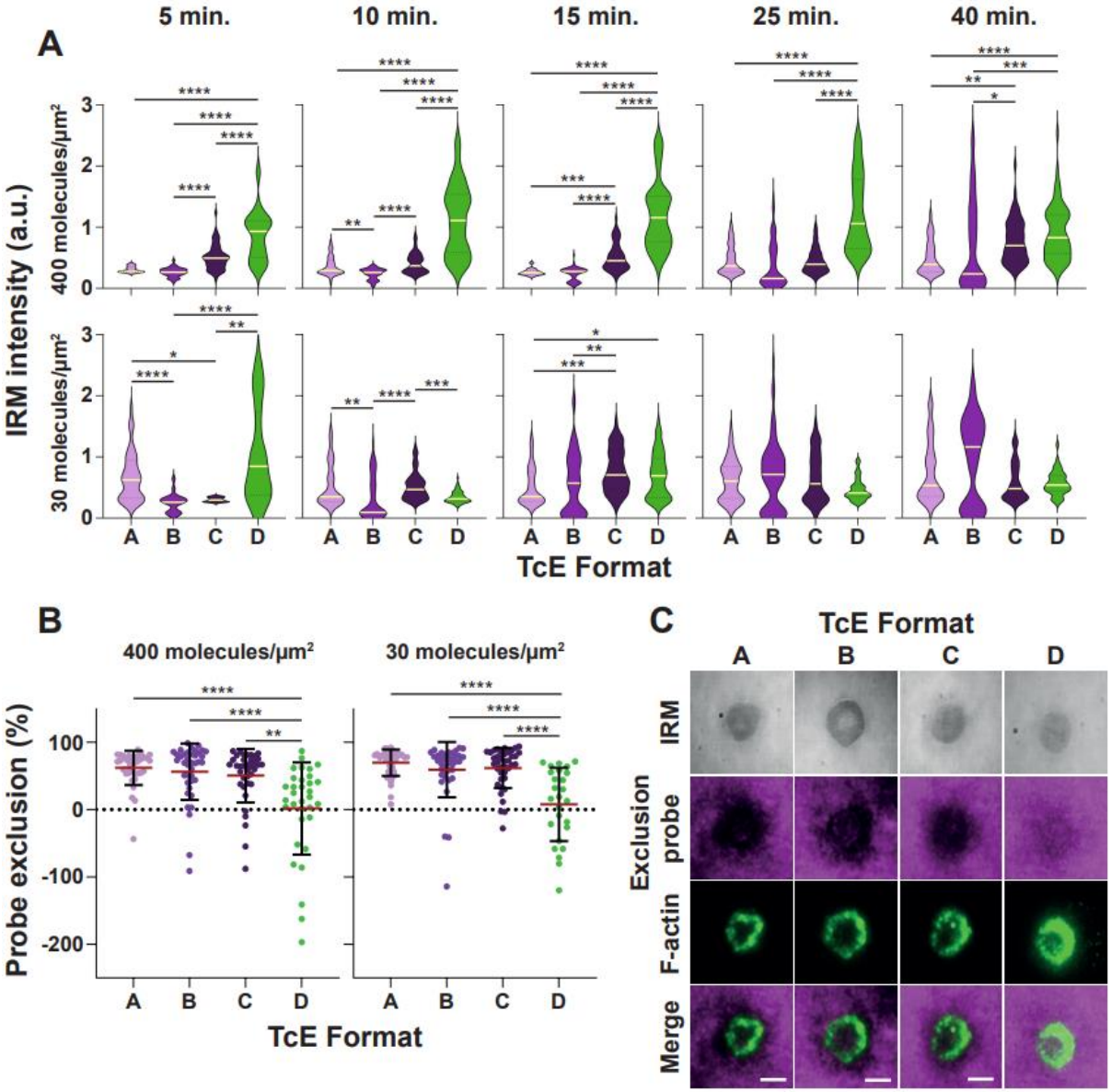

Figure 4. **TcE-mediated T cell-SLB intermembrane spacing and molecular exclusion.** (**A**) Time-resolved, relative IRM intensity at the TcE-mediated IS at 400 (top) or 30 (bottom) molecules/µm^2 of Her2. Yellow solid line = median, Grey dashed line = quartiles. 2 biological replicates. Kruskal-Wallis test. * $p<0.05$, ** $p<0.005$, *** $p<0.0005$, **** $p<0.00005$. (**B**) Probe exclusion compared to background levels in percent at the TcE mediated IS at 400 (left) or 30 (right) molecules/µm^2 of Her2. Mean (solid red line) ± SD (solid black lines). Dotted black line indicates no exclusion. Negative values refer to probe accumulation. 2 biological replicates, Kruskal-Wallis test, ** $p<0.005$, **** $p<0.0005$. (**C**) Representative TIRF and IRM images of TcE mediated IS formation on SLBs containing exclusion probe (magenta) at 400 molecules/µm^2 of Her2, stained for F-actin (magenta), scale bars = 5µm.

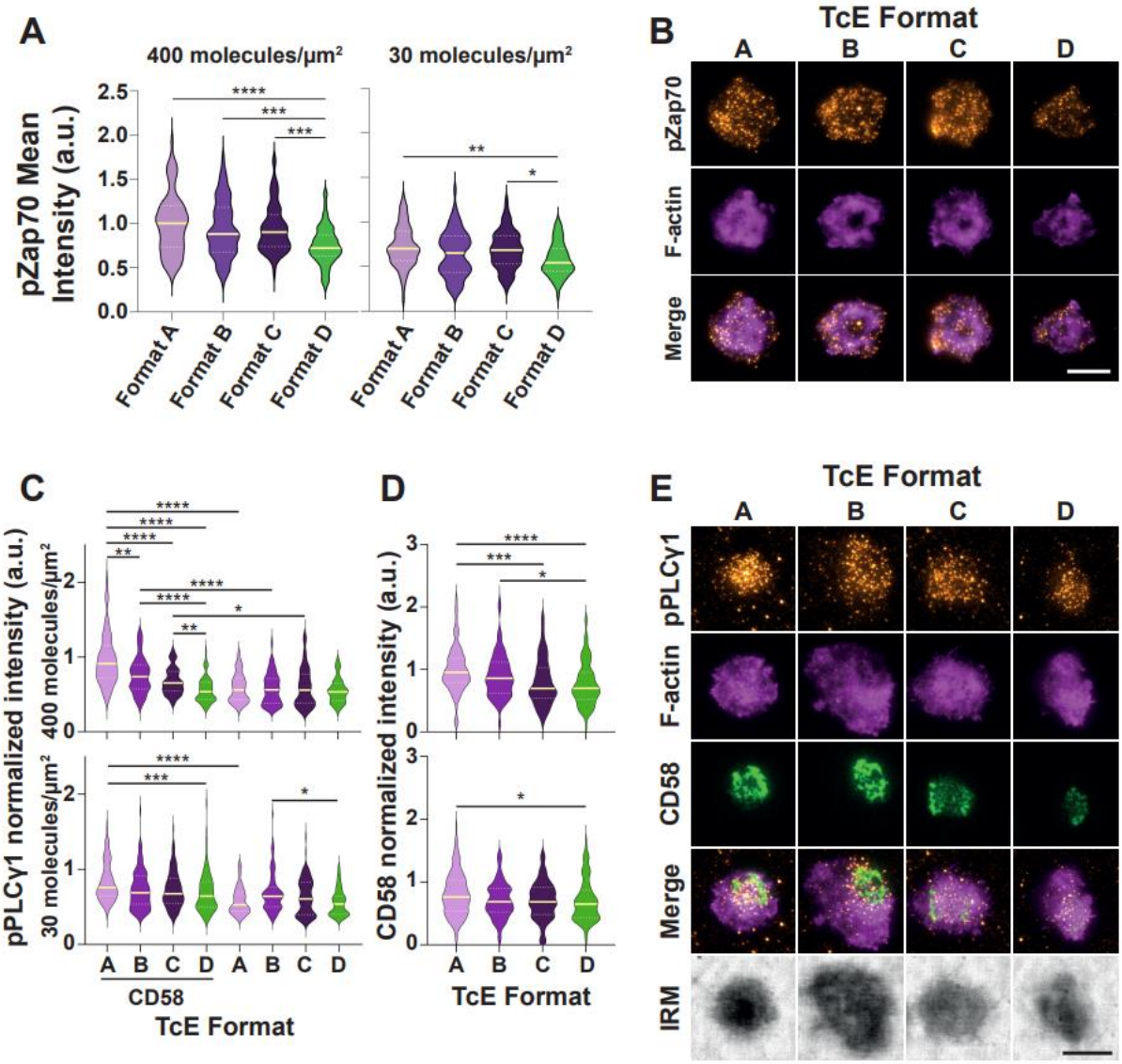

Figure 5. **TcE-mediated signalling.** (**A**) Normalized pZap70 levels at the TcE-mediated IS at 400 (left) or 30 (right) molecules/µm^2 of Her2. Yellow solid line = median, White dashed line = quartiles. 2 biological replicates, Kruskal-Wallis test, * p<0.05, ** p<0.005, *** p<0.0005, **** p<0.0005. (**B**) Representative TIRF images of TcE mediated IS formation on SLBs at 400 molecules/µm^2 of Her2 after 20min. of interaction, stained for F-actin (magenta) and pZap70 (orange), scale bar = 5µm. (**C**) Normalized pPLCγ1 levels at the TcE-mediated IS at 400 (top) or 30 (bottom) molecules/µm^2 of Her2 in the presence or absence of CD58. Yellow solid line = median, White dashed line = quartiles. 2 biological replicates, Kruskal-Wallis test, * p<0.05, ** p<0.005, *** p<0.0005, **** p<0.0005. (**D**) Normalized CD58 levels at the TcE-mediated IS at 400 (top) or 30 (bottom) molecules/µm^2 of Her2 in the presence of CD58. Yellow solid line = median, White dashed line = quartiles. 2 biological replicates, Kruskal-Wallis test, * p<0.05, *** p<0.0005, **** p<0.0005. (**E**) Representative TIRF and IRM images of TcE mediated IS formation on SLBs at 400 molecules/µm^2 of Her2 in the presence of CD58 (green) after 20min. of interaction, stained for pPLCγ1 (orange), F-actin (magenta), scale bar = 5µm.